Optimization of the operational domain for ICRH scenarios in WEST from statistical analysis

D. Moiraf, J. Morales, L. Colas, N. Fedorczak, J. Gaspar, R. Dumont

Optimization of the operational domain for ICRH scenarios in WEST from statistical analysis

D. Moiraf, J. Morales, L. Colas, N. Fedorczak, J. Gaspar, R. Dumont and the WEST team*

CEA, IRFM, F-13108 Saint-Paul-lez-Durance, France

E-mail: david.moiraf@cea.fr

*See http://west.cea.fr/WESTteam for the list of team members.

May 2023

Abstract.

In the WEST tokamak, the Ion Cyclotron Resonance Heating (ICRH) system plays a substantial role in increasing the plasma temperature. However, its efficiency can be lowered by two main phenomena: ripple-induced fast ion losses and technical limits on the antenna current. In this work, a new technique using IR thermography was employed to measure the flux of particles coming from the trapping of fast ions in the toroidal magnetic field ripple. These measurements provided the opportunity to fit parametric scaling laws in order to predict the ion flux intensity and the total power loss for experiments with a plasma current of $I_p = 500\ kA$ and a major radius of the cyclotron resonance layer of $R_{1H} = 2.5\ m$ depending on the heating power and the line-averaged electron density. Furthermore, another semi-empirical parametric scaling was developed to evaluate the coupling resistance depending on controllable parameters such as the line averaged electron density and the radial outer gap between the separatrix and the ICRH antenna. These laws were used to define an operational domain from the database of previous experiments made during campaign C4. The settled operational domain suggests that high power ($P_{icrh} > 3\ MW$) and high electron density ($\overline{n_e} > 5.0\ 10^{19}\ m^{-3}$) discharges are suitable for optimized steady-state high confinement scenarios in WEST using ICRH.

Keywords: tokamak, scaling law, fast ion, ripple, coupling, optimization, operation, icrh, icrf, scenario, west

1. Introduction

The Tungsten (W) Environment in Steady-state Tokamak (WEST) is a major upgrade of the superconducting medium-size tokamak Tore Supra [1, 2, 3]. Its main parameters are a major radius $R_0 = 2.4$ m, a minor radius $a = 0.5$ m, a toroidal magnetic field $B_T = 3.8$ T, and a plasma current up to $I_p = 1$ MA. WEST was designed with the intention of testing and minimizing risks for ITER divertor procurement and operation. The divertor has to undergo a substantial and continuous heat flux in order to measure the robustness of the tungsten monoblocks that will pave ITER's divertor.

One of the main WEST objectives is to find a steady-state high confinement scenario using the Ion Cyclotron Resonance Heating (ICRH) heating system. This system increases the plasma temperature by using intense Radio-Frequency (RF) electric fields resonant with the cyclotron motion of a minority ion species at the plasma center. However, several issues can lead to power loss or non-efficient transfer of power. Two main issues are identified:

- The discrete number of coils create a modulation of the toroidal magnetic field along the toroidal direction. This modulation called *magnetic ripple* creates local wells that can trap particles if the ratio between perpendicular to parallel speed is high enough. Because ICRH tends to increase the perpendicular speed of the ions, it is also responsible for the higher loss of these particles. Ripple-induced fast ion losses can represent tens of percent of the input power and lead to the overheating of the plasma-facing components.
- For the coupling between the ICRH wave and the plasma to be efficient, a high plasma coupling resistance is recommended. Low coupling resistance can cause the current in the antenna matching capacitor to be too high when requesting large ICRH power, triggering a feedback controller that reduces the power to stay below the operational limit [4]. This parameter is dependent on the edge electron density and the distance between the fast-wave cut-off layer and the antenna.

In this paper, each of these issues will be described and measured in section 2 and 3 respectively. Using the reduced WEST database as in [5], scaling laws are developed in order to predict the influence of a few controllable plasma parameters regarding these phenomena. Finally, in section 4, we define a 2D operational domain in density/ICRH power space that limits each effect and optimizes ICRH scenarios for robust steady-state high confinement experiments in WEST. However, this study is limited to the standard D[H] minority heating scenario in dipole strap phasing for experiments with a plasma current of $I_p = 500\ kA$ and a major radius of the cyclotron resonance layer of $R_{1H} = 2.5\ m$. This optimization exercise is focused on ICRH and complements other optimization studies performed on WEST, focusing on impurities [5] and the Lower-Hybrid Current Drive (LHCD) [6].

2. Ripple-induced losses

2.1. Fast ion losses in magnetic ripple

The finite number of toroidal coils leads to a modulation $\delta = (B_{max} - B_{min})/(B_{max} + B_{min})$ of the toroidal magnetic field taken along the toroidal angle at a given (R, Z). The intensity of the field between two coils is smaller than the field under a coil. The periodicity of this modulation is $2\pi/N$ with N being the number of toroidal coils. As the distance between the coils increases with the major radius, also does the modulation. In WEST, δ can reach up to 2.3% at the plasma edge ($R = 2.93$). Fig.1 shows the evolution of the toroidal magnetic field amplitude depending on the toroidal angle of a particle along its trajectory on the plasma periphery.

Trapping can take place in local wells created by the magnetic ripple. A particle is locally trapped if its ratio of perpendicular to parallel speed $v_\perp/v_\parallel$ is high enough. Fast ions trapped in banana orbits with turning points in the region of high modulation (meaning $v_\parallel = 0$) have a high probability of being trapped in a local magnetic mirror. When locally trapped, as the rotational transform is no longer playing a role, these ions drift out of the plasma on a short timescale. Low-energy ions are frequently de-trapped by collisions and can therefore not be assumed to be promptly lost. It is mostly fast ions, heated via ICRH (as the heating increases $v_\perp$), that are lost. In WEST, the super-trapped ions then follow the iso-B lines towards the baffle and transfer their energy in the form of heat. This is why periodically symmetric

hot areas are observed on the baffle as shown in Fig 2. In this study, we suppose no fast ion is reflected at the baffle surface, and 100% of the energy is transferred in the form of heat.

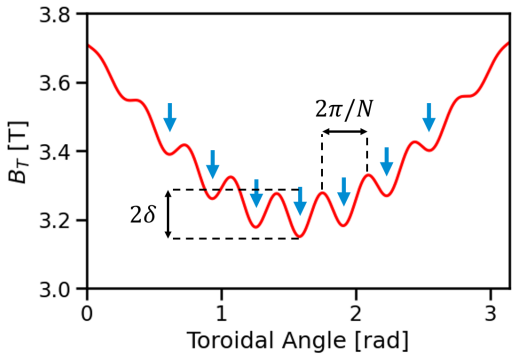

Figure 1. Evolution of the toroidal magnetic field as a function of the toroidal angle along a particle trajectory at the plasma edge of Tore Supra ($\delta = 5\%$), similar in WEST. Blue arrows point to the local wells where fast ions can be trapped and lost.

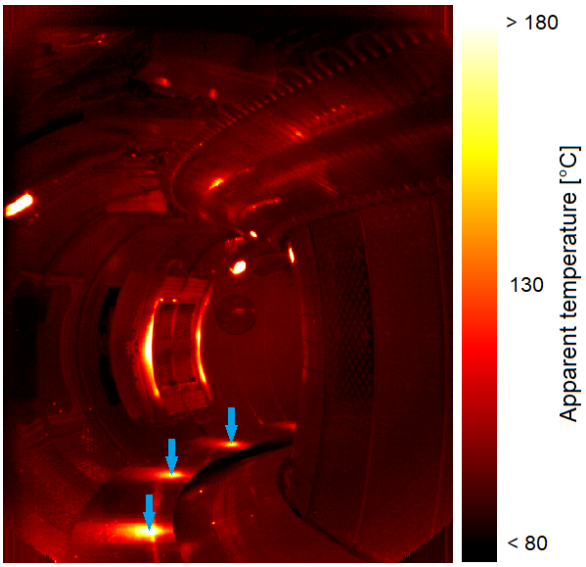

Figure 2. Infrared image from the inside of the vacuum vessel taken with WEST wide-angle infrared diagnostic [7]. Blue arrows show the periodic hot areas due to ripple-induced fast ion losses on the baffle, left to the lower divertor. Picture from discharge number 55604 at t = +8s (during plasma). The temperature scale is given in Black Body temperatures and does not represent the real surface temperature of the plasma-facing components.

2.2. Evaluation of the local and integrated power loss in the magnetic ripple

Particles trapped in ripple wells will drift vertically downward until they hit the baffle and transfer their energy in the form of heat. As the tiles temperature increases, more photons in the wavelength visible from Infra-Red (IR) diagnostics are collected. An actively cooled optical endoscope looking down at the lower divertor with a resolution of 2.8mm per pixel allows the monitoring of the baffle components. The IR camera setup is detailed in reference [8]. The baffle surface temperature is calculated using a similar method as in references [9, 10]. From the evolution of the temperature radial profile given by the IR thermography and a thermal model of the inertial baffle, the ripple-induced fast ion flux q_{dep} is evaluated using the code TEDDY [11]. Some uncertainties raise from the evaluation of the surface temperature. A Monte Carlo scheme has been used to evaluate the variation in the calculation of q_{dep}. The details of the quantification of ripple-induced losses are available in the appendix. Fig.3 shows the temporal evolution of the radial temperature profile and the radial heat flux profile (output from TEDDY).

To better visualize the results, the plot in Fig.4 only exhibits the temporal evolution of q_{dep} on the radius where the maximum flux has been reached. This graph allows to directly compare the heat flux to the ICRH power, exhibiting the strong correlation between the two quantities, as expected from the theory. In the absence of ICRH, no signal more intense than the noise has been measured. ICRH power P_{ICRH} is defined as the forward ICRH power minus the reflected ICRH power.

From the calculation of the flux q_{dep}, the total power due to ripple-induced trapping P_{ripple} is evaluated by integration. The flux is assumed to form a 2D Gaussian as shown in Fig.5. Fitting q_{dep} with a Gauss bell has two advantages: On the one hand, it reduces the number of variables defining the profile to the amplitude $A_{dep}(t)$, and the width σ. On the second hand, it allows to take into account the power flux deposited outside the measured region (i.e. outside the camera's field of view or on the divertor) by extending the profile. The total power lost in ripple-induced trapping is calculated as follows:

$$P_{ripple}(t) = 2\pi\ A_{dep}(t)\ \sigma^2 \times 18$$

The result is multiplied by 18 to take into account the 18 toroidal coils (and thus hot areas) in WEST. Because the fitting works better with higher flux and because the dependency follows σ^2, we consider σ constant during a pulse to limit the fluctuations. To compute its value, a median is taken from the Gaussian fits where the Root Mean Square Error (RMSE) is below a threshold and the ICRH power is above 1 MW. Details on the error in the estimate of the deposited flux induced by these approximations are given in annex, section 9. For discharge 55604, the total lost power due to ripple-induced trapping of ions is shown in Fig.6.

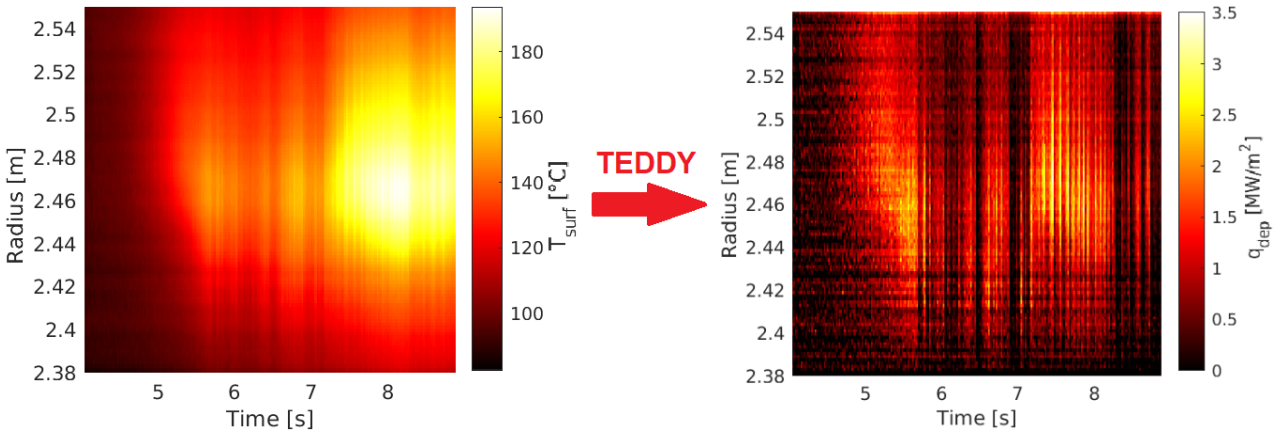

Figure 3. Left: Baffle tile measured surface temperature T_{surf} as a function of (t, R) during discharge 55604. Right: Fast ion flux intensity q_{dep} as a function of (t, R) calculated with TEDDY during the same discharge. During WEST campaign C4, the tiles were not actively cooled, meaning the temperature profile shows thermal inertia (taken into account in TEDDY).

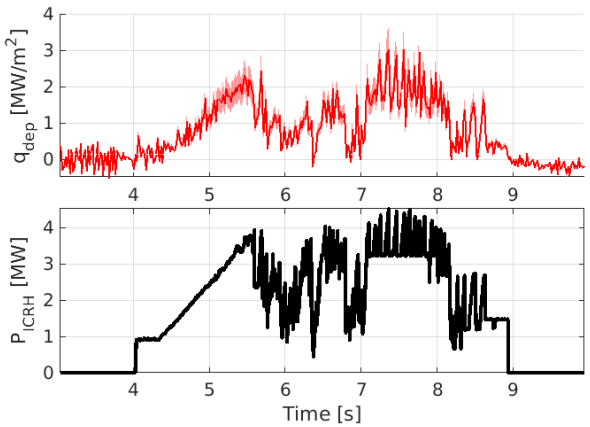

Figure 4. Top: Temporal evolution of the power deposition q_{dep} at $R = 2.47m$ with error bars. Bottom: Temporal evolution of the ICRH heating power for discharge 55604.

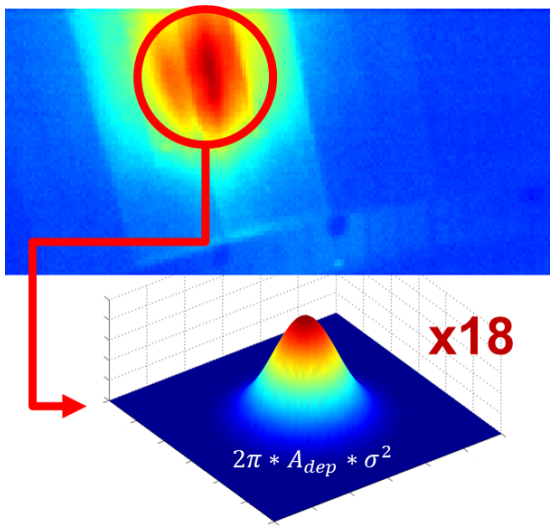

Figure 5. Image from the upper IR camera during discharge 55604 and illustration of the 2D gaussian approximation.

2.3. Parametric scaling law of ripple-induced losses

The same study is performed on 53 pulses showing ripple-induced losses on the IR diagnostics. Each one of them gives a signal q_{dep} or P_{ripple} that can be compared to other parameters using the reduced WEST database. This database takes the average or median values of the discharge parameters on *plateaus*. Plateaus are time intervals where the total heating power and the plasma current are constant (with an allowed fluctuation of 5% around the averaged value). In these conditions, the plateaus can be considered "quasi-steady-state", meaning the ripple-induced losses can be considered constant and different parameters can be linked to one another easily. From the 53 discharges, 41 plateaus are extracted. Counter-intuitively, the number of plateaus is smaller than the number of discharges because a few ICRH plasmas from our database are not steady-state for long enough to have a detectable plateau, mainly due to coupling issues, such as the discharge 55604 shown in Fig.6.

Previous modeling of ripple losses in Tore Supra [12] shows that losses are affected by the ICRH power P_{ICRH}, the core electron density $\overline{n_e}$, the plasma current I_p, the isotopic ratio n_H/n_D and major radius of the hydrogen cyclotron resonance layer R_{1H}. At $R = R_{1H}$, the RF field is resonant with the local cyclotron motion of hydrogen minority ions. Since trapped ions spend most of their bounce time near their banana tips, they are mostly located at this major radius. Even though the plasma current I_p should increase the size of the good confinement region, no correlation has been found in Tore Supra [13], and not enough data is available in our database to correctly identify its dependency. Same issue with

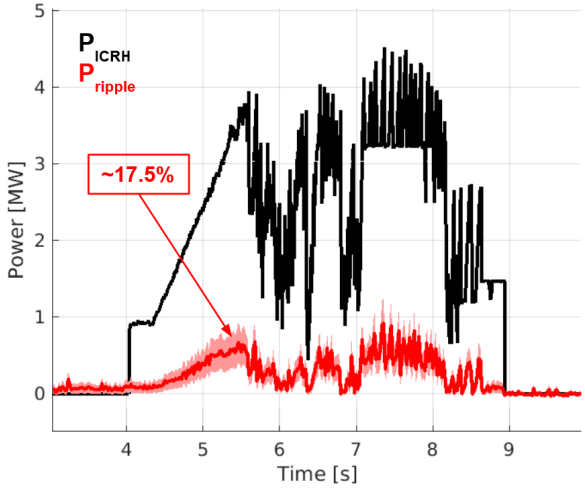

Figure 6. Comparison between the total power loss due to magnetic ripple P_{ripple} and the ICRH power P_{ICRH} during pulse 55604. Here, at maximum, $P_{ripple}/P_{ICRH} \simeq 17.5 \pm 7.1\%$.

the parameter R_{1H}, where not enough data points at high ICRH power exist to assess its role. For this reason, this study only focuses on experiments with $I_p = 500$ kA and $R_{1H} = 2.5$ m. Besides, with the isotopic ratio ranging from 0% to 12% in the database, no clear dependence with ripple-induced losses was found. As this parameter is strongly correlated to the plasma density in our database, it has been chosen to not consider it as it tends to increase uncertainty. Taking into account the previous points, we now turn to scaling laws for the local and total ripple-induced loss evaluation. These laws have been obtained by fitting the exponents minimizing the RMSE between the scaled values and the measured power.

$$q_{dep}\ [MW/m^2] = 247\ P_{ICRH}^{\alpha_1}\ [MW]\ \overline{n_e}^{\beta_1}\ [10^{19}\ m^{-3}]$$

with the exponents $\alpha_1 = 1.26 \pm 0.30$ and $\beta_1 = -4.55 \pm 0.86$, and:

$$P_{ripple}\ [MW] = 2.48\ P_{ICRH}^{\alpha_2}\ [MW]\ \overline{n_e}^{\beta_2}\ [10^{19}\ m^{-3}]$$

with the exponents $\alpha_2 = 1.36 \pm 0.27$ and $\beta_2 = -2.16 \pm 0.76$. One should keep in mind that the values of the exponents are specific to WEST with discharges at $I_p = 500\ kA$ and $R_{1H} = 2.5\ m$. For the general reader, the important feature is the trend and not the absolute number. The exponents' uncertainties are given by the statistical error bars and do not take into account the error bars on the measured plasma parameters. Comparison between measured values and calculated ones using the scaling laws is shown in Fig.7

The lost power increases somewhat faster than the injected power. It should be a consequence of the larger transmitted power per resonating ions. Fortunately, these losses can be mitigated by increasing the central electron density, as they are inversely proportional to

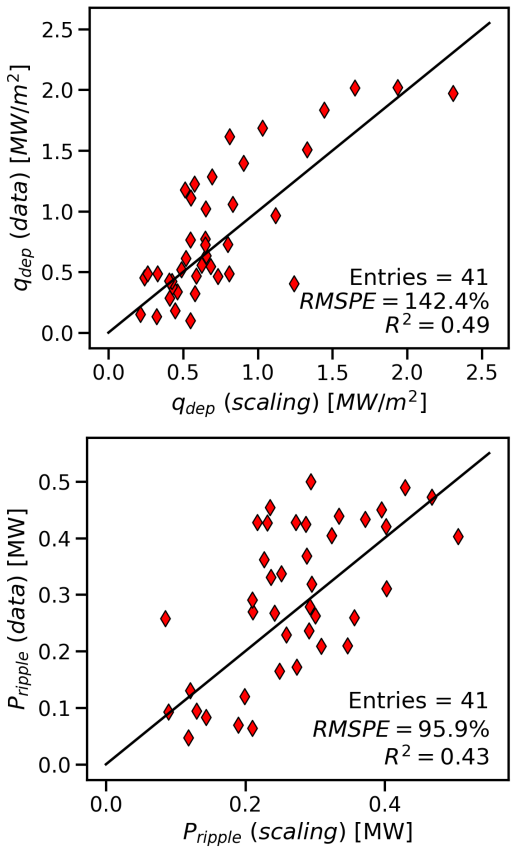

Figure 7. Comparisons between the calculated parameter from the scaling law and the measured value. Top figure is for the power deposition q_{dep} and bottom one is for the power loss P_{ripple}. Black lines show a x=y function. The closer the markers are to the black line, the better the scaling law.

the squared value of this parameter. This result can be summarized in the parameter space ($\overline{n_e}$, P_{ICRH}) in Fig.8. The markers correspond to data points (plateaus) and their coloration is linked to the color of the iso-lines P_{ripple}/P_{ICRH}. Some discrepancies are visible due to the statistical nature of this law.

The scaling law for P_{ripple} can be compared to the one previously developed for Tore Supra [14], provided below for the conditions $I_p = 500\ kA$ and $R_{1H} = 2.5\ m$:

$$\langle E_{ripple} \rangle\ [keV] = 8 \times \frac{P_{ICRH}\ T_{e0}^{3/2}}{n_H(0)\ \overline{n_e}} + 150$$

$$I_{ripple}\ [mA] = 18 \times 208.18\ P_{ICRH}^{1.01}\ n_l^{-0.87}$$

$$P_{ripple}\ (Basiuk)\ [MW] = \langle E_{ripple} \rangle\ [keV] * I_{ripple}\ [mA]$$

with P_{ICRH} the ICRH power in [MW], T_{e0} the central electron temperature in [keV], n_l the line integrated electron density in $[10^{19}\ m^{-2}]$, $n_H(0)$ the central hydrogen density and $\overline{n_e}$ the core electron density, both in $[10^{19}\ m^{-3}]$. $\langle E_{ripple} \rangle$ correspond to the average fast ion energy and I_{ripple} the current of fast ion entering a previously existing diagnostic called DRIPPLE-I [15].

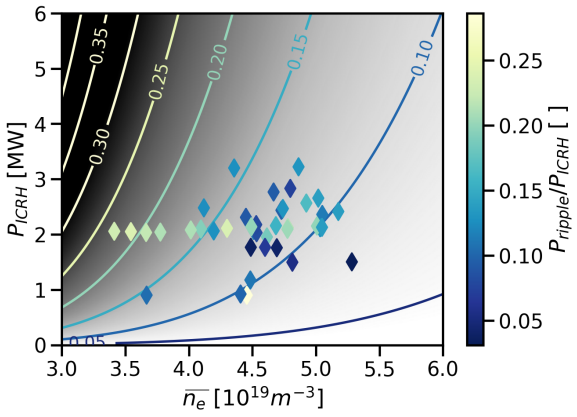

Figure 8. Parameter space showing the location of the 41 plateaus used for the construction of the scaling law. The coloration of the markers and iso-lines correspond to the ratio P_{ripple}/P_{ICRH}. The darker the background, the more ripple-induced losses are expected.

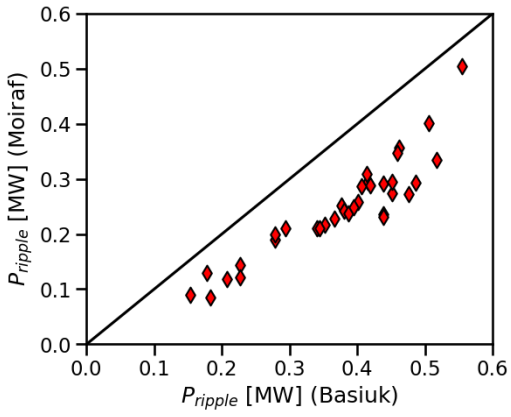

Figure 9. Comparison of the total power lost by fast ion ripple losses P_{ripple}, calculated by IR thermography (vertical) and Tore Supra scaling law (horizontal) [14]. The black line shows the x=y function.

From the same database, the results of both equations are displayed in Fig.9. Data points seem to align pretty well but show a slight overestimation from Tore Supra scaling law. This can be explained by several factors. Tore Supra and WEST are quite different devices (plasma size, shape, plasma-facing components...), so it is not surprising to find a discrepancy. However, other explanations are possible. The scaling law for Tore Supra was built around a specific diagnostic system [13] that directly measured the current coming from the ion flux and does not rely on IR thermography. The reflection coefficient may not be negligible as we supposed in this paper, meaning the underestimation comes from our side. Another explanation would be that for Tore Supra's law to work, one needs to evaluate the average energy of the fast ions. Reducing this energy by 50 keV completely erases the discrepancy between the two relations. The evaluation of fast ion average energy is out of the scope of this paper, so no interpretation will be given here. The important information to keep in mind is that the measured trend is completely similar.

By limiting the ripple-induced power loss to a certain percentage of the ICRH input power labelled f_{ripple}, it is possible to determine a condition on P_{ICRH} depending on $\overline{n_e}$:

$$P_{ICRH} < \left(\frac{f_{ripple}\ \overline{n_e}^{-\beta_2}}{2.48} \right)^{1/(\alpha_2 - 1)} \quad (1)$$

However, the real problem would be to cross the thermal limit of the baffle components. According to [16], the copper tiles operation is not assured for a heat flux higher than $q_{lim} = 3MW/m^2$ during an extended period. This value creates an operational limit of P_{ICRH} as a function of the $\overline{n_e}$:

$$P_{ICRH} < \left(\frac{q_{lim}\ \overline{n_e}^{-\beta_1}}{247} \right)^{1/(\alpha_1)} \quad (2)$$

3. ICRH and plasma coupling

3.1. Parametric scaling of the coupling resistance

The higher the wave coupling resistance $\mathfrak{R}_c$, the better the ICRH coupling efficiency. Low coupling resistance can be a limiting factor on the coupled power, as the forward power is feedback-controlled to keep the currents in the antenna matching capacitors lower than 915 A [4]. To increase this parameter, it is necessary to build a scaling law that can link $\mathfrak{R}_c$ to configurable operational parameters.

The main determinant of the ICRH wave coupling physics is the evanescence of the fast wave between the straps located at R_{strap} and the typical peripheral R_{cutoff} layer for the main wave number $k_{//}$ excited by the antenna. This assumption is supported by antenna modeling, as well as earlier experimental studies in several machines using detailed edge density profiles [17, 18, 19]. Along this line of thought, one can expect the coupling resistance to be of the form:

$$\mathfrak{R}_c \propto exp\left(-\frac{R_{strap} - R_{cutoff}}{L_E} \right)$$

In this expression, R_{cutoff} is the radial location of the cut-off layer and R_{strap} the radial position of the radiating straps (in the plasma mid-plane), while L_E is a typical decay length to be estimated experimentally. The straps remain at a fixed radial distance from the leading edge of the ICRH antenna limiters, whose radial position R_{ant} is stored for each pulse in the WEST database. So, instead of R_{strap},

R_{ant} may be used in a scaling law and incorporate the fixed extra factor $exp((R_{strap} - R_{ant})/L_E)$ into a constant $\mathfrak{R}_{c0}$. For dipole strap phasing the main $k_{//}$ in the coupled spectrum is typically $9m^{-1}$, and the R_{cutoff} density at that $k_{//}$ for standard D[H] minority heating is $n_{cutoff} \sim 0.9\ 10^{19}\ m^{-3}$. Ideally, one should deduce R_{cutoff} from detailed edge density profiles (see [18]). Alternatively, the electron density profiles can be written formally as:

$$n_e(R) = n_{e0}\ F(R - R_0)$$

$$\Rightarrow R_{cutoff} = R_0 + F^{-1}\left(\frac{n_{cutoff}}{n_{e0}}\right)$$

where R_0 is the radius of the magnetic axis, n_{e0} the central electron density and F a profile shape function. We now assume that the R_{cutoff} layer remains radially close to the magnetic separatrix at R_{sep} as the plasma current is the same between the studied discharge. Note that the separatrix does not play a specific role in the ICRH coupling physics, but R_{sep} is generally a controlled parameter of the discharge that is convenient for the database. One can locally assimilate the profile shape to a line:

$$R_{cutoff} \sim R_{sep} + \lambda_n\left(1 - \frac{n_{cutoff}}{n_{sep}}\right)$$

where n_{sep} is the density at the separatrix and $\lambda_n \equiv -F(R_{sep} - R_0)/F'(R_{sep} - R_0) > 0$ is the local density gradient length at the separatrix. Inserting this ansatz into the expression of $\mathfrak{R}_c$ yields:

$$\mathfrak{R}_c \sim \mathfrak{R}_{c0}\ exp\left(-\frac{R_{ant} - R_{sep}}{L_E} + \frac{\lambda_n}{L_E} - \frac{\lambda_n}{L_E}\frac{n_{cutoff}}{n_{sep}}\right)$$

In the argument of the exponential, the first term $exp(\lambda_n/L_E)$ may be incorporated into $\mathfrak{R}_{c0}$, as λ_n can be supposed almost constant for a constant plasma current $I_p = 500kA$. As a proxy for the density at the separatrix, one may use the density $\overline{n_{edge}}$ integrated along a peripheral line of sight #2 of the interferometer passing through the edge plasma [20]. The Radial Outer Gap $R_{ant} - R_{sep} = ROG_{avg}$ corresponds to the average distance between the separatrix and the antenna taken at the upper (Z=+25cm), middle (Z=0cm) and lower (Z=-25cm) plane of the antenna. In summary, we propose to seek a semi-empirical parametric dependence of the form:

$$\mathfrak{R}_c \sim \mathfrak{R}_{c0}\ exp\left(-\frac{ROG_{avg}}{L_E} - \frac{n_c}{\overline{n_{edge}}}\right) \quad (3)$$

with $\mathfrak{R}_c$ and $\mathfrak{R}_{c0}$ in $[\Omega]$ ROG_{avg} and L_E in [cm] and n_c and $\overline{n_{edge}}$ in $[10^{19}\ m^{-3}]$. We define $n_c = \lambda_n n_{cutoff}/L_E$. In this proposed expression, one needs to fit the three unknown parameters $\mathfrak{R}_{c0}$, L_E, and n_c from the measurements over the reduced WEST database.

3.2. Scaling from experimental data

The coupling resistance $\mathfrak{R}_c$ in the database is deduced from voltage measurements in the antennas as explained in [4]. It corresponds to the average value of the coupling resistance of the 4 straps composing the antenna Q4 (where more data points are available). Thus, it is supposed that the coupling resistance is the same for all the straps in WEST. Fitting equation (3) with plateaus with ICRH power in the reduced WEST database, the minimization of the RMSE gives the following coefficients:

- $\mathfrak{R}_{c0} = 3.76 \pm 0.41\ \Omega$
- $L_E = 5.11 \pm 0.42\ cm$
- $n_c = 1.41 \pm 0.19\ 10^{19}\ m^{-3}$

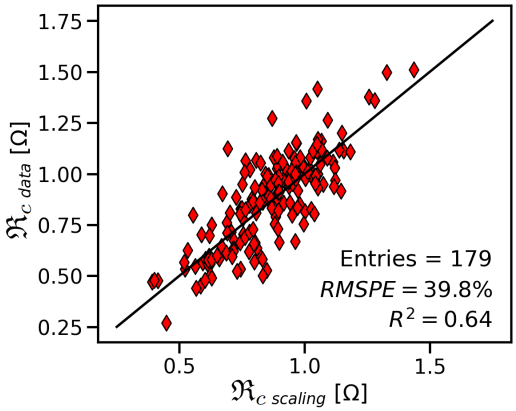

Figure 10. Comparison between the coupling resistance calculated from the scaling law $\mathfrak{R}_{c\ scaling}$ and from voltage measurements $\mathfrak{R}_{c\ data}$. The black line shows the x=y function. The closer the markers are to the black line, the better the scaling law.

Again, the values of the exponents are specific to WEST with discharges at $I_p = 500\ kA$ and $R_{1H} = 2.5\ m$. The uncertainties are given by the statistical error bars and do not take into account the error bars on the measured plasma parameters. Comparison between measured values and calculated ones using the scaling law is shown in Fig.10.

To better understand these results, similarly to the Fig.8, the Fig.11 shows a parameter space (ROG_{avg}, $\overline{n_{edge}}$). The markers correspond to data points (plateaus) and their coloration is linked to the value of the coupling resistance $\mathfrak{R}_c$.

As shown in Fig.11, the coupling resistance is highly dependent on ROG_{avg}. In all previous magnetic configurations, the shaping of the separatrix was not conformed to the antenna poloidal shape (more "peaked" at the outer mid-plane). This means that the radial outer gap at the upper and lower plane of the antenna was larger. By better shaping the separatrix

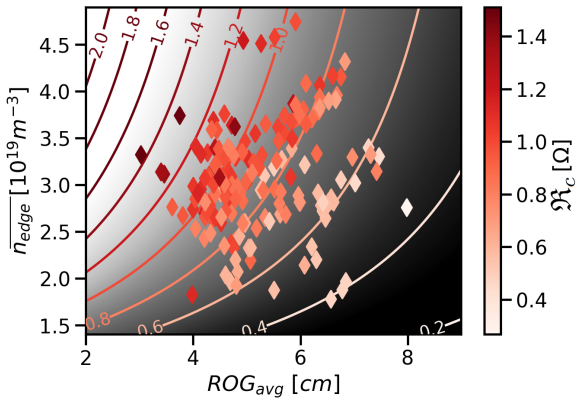

Figure 11. Parameter space showing the location of the 179 plateaus used for the construction of the scaling law. The coloration corresponds to the coupling resistance $\mathfrak{R}_c$. The darker the background, the lower the coupling resistance.

to match the curvature of the antenna, ROG_{avg} can be reduced without having the plasma closer to the antenna (that could enhance the generation of tungsten impurities coming from the antenna limiters). $\overline{n_{edge}}$ corresponds to the line averaged edge density, which is not currently a control parameter in WEST. Fortunately, this value is linked to the line averaged core electron density (controlled in real-time) $\overline{n_e}$ with a linear equation $\overline{n_{edge}} = 0.70\ \overline{n_e}$ as seen in Fig.12.

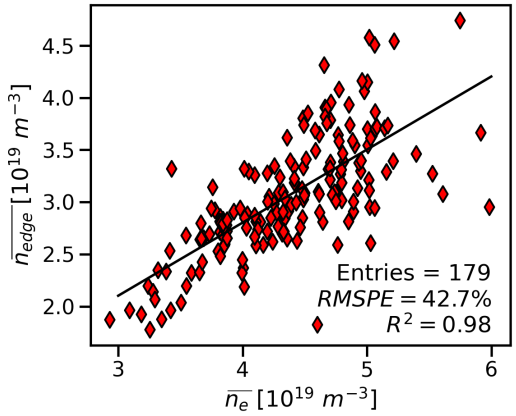

Figure 12. Linear dependency between the line averaged edge electron density $\overline{n_{edge}}$ and the line averaged central electron density $\overline{n_e}$. From the reduced WEST database, we obtain $\overline{n_{edge}} = 0.70\ \overline{n_e}$.

3.3. Limit on the matching capacitors current

The coupling resistance is an important parameter as it determines the maximum ICRH power available in the systems' operational domain. Indeed, the ICRH power generated by one strap P_{strap} can be written as:

$$P_{strap} = \frac{1}{2}\mathfrak{R}_c I_{capa}^2$$

where $\mathfrak{R}_c$ is the coupling resistance in [Ω] and I_{capa} the current passing through the ICRH matching capacitors in [A]. The operation of these capacitors is not guaranteed for a current higher than $I_{lim} = 915\ A$ [4], limiting the maximum P_{strap}. WEST has 3 antennas, each containing 2x2 straps, but the top and bottom straps on each side of the antenna are connected together. The coupling resistance given in the database is an average of top and bottom coupling resistances. By supposing that $P_{strap} = \frac{1}{12}P_{ICRH}$ we are left with the condition:

$$P_{ICRH} < 6\ \mathfrak{R}_c(ROG_{avg}, \overline{n_e})\ I_{lim}^2 \tag{4}$$

This new limit on P_{ICRH} is in fact highly sensitive to ROG_{avg}, as shown in Fig.13.

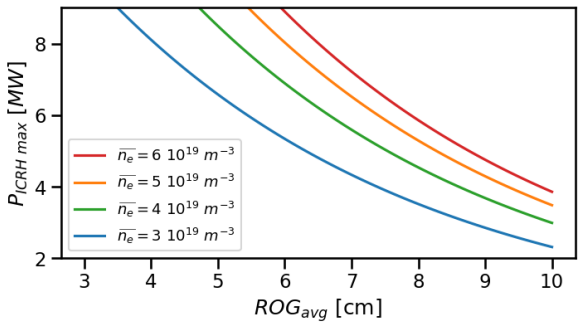

Figure 13. Evolution of the ICRH power limit calculated from equation (4) depending on the averaged radial outer gap ROG_{avg} and for different values of line averaged core electron density $\overline{n_e}$.

These limits suppose that the coupling resistance and the currents are equal for all the straps. In reality, the currents between the straps of an antenna can be unbalanced due to the plasma non-uniformity and capacitor tuning. If one strap reaches the limit in current, the power in the whole antenna is reduced, meaning that experimentalists can observe a power reduction even for $ROG_{avg} < 6cm$. However, equation (4) is still useful to determine a theoretical threshold that cannot be crossed even in a perfectly uniform scenario. For the rest of this work, the ROG_{avg} will be fixed at 8cm and 6cm for simplification, but readers should keep in mind that the limit is strongly sensitive to this parameter and can be pushed further.

4. Operational domain

In a parameter space (P_{ICRH}, $\overline{n_e}$), the previously calculated scaling laws allow drawing two limits beyond which the flux due to ripple-induced losses is too high (equation (1)) or beyond which the current in the capacitors of the ICRH system is too high (equation (4)). Also, the ripple-induced power loss has been arbitrarily limited to $P_{ripple} < 10\%\ P_{ICRH}$ in equation

(2) but does not constitute a hard boundary (even less for an actively cooled baffle). To these we can add the Greenwald density limit [21] which for WEST is equal to $n_G = I_p/(2a^2) = 6.37\ 10^{19}\ m^{-3}$ at $I_p = 0.5\ MA$. All these conditions are drawn in a parameter space to show the operational domain during ICRH experiment in Fig.14.

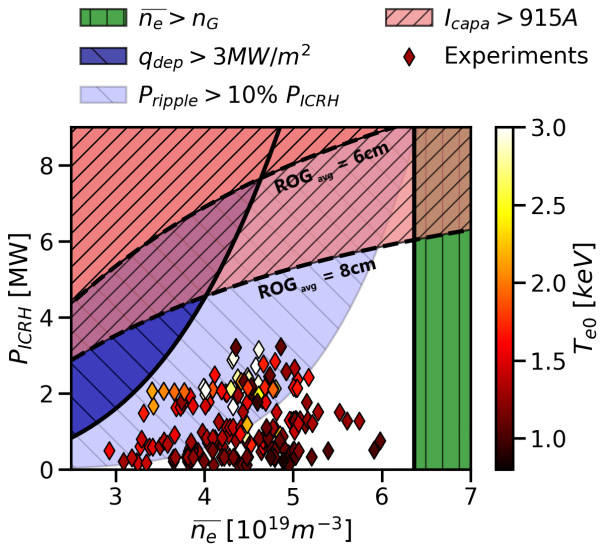

Figure 14. Parameter space (P_{ICRH}, n_e) with different limits deduced from the scaling laws presented in equations (1,2,4). The scattered markers correspond to plateaus with ripple-induced losses or plateaus using only ICRH as auxiliary heating. Each is colored by the measured central electron temperature T_{e0}.

Some plateaus that should have a high central electron temperature T_{e0} are cold, mostly due to W impurity contamination [5]. One should not forget that the limit due to the capacitor current can be pushed further up by changing the ROG_{avg} as seen in Fig.13. With a smaller ROG_{avg}, the main limiting phenomena would be the ripple-induced losses. This graph shows that for high ICRH power experiments ($P_{ICRH} > 4MW$), the ROG_{avg} should be shorter than 8cm and a minimum electron density of 5.0 $10^{19} m^{-3}$ should be aimed.

5. Conclusions

The IR thermography system allowed to measure ripple-induced fast ion losses due to the use of ICRH in WEST. By adding this data to the reduced WEST database and developing new scaling laws to, not only predict ripple-induced fast ion losses, but also the plasma coupling resistance, a new operational domain has been determined. This parameter space draw a valley of operation that will help experimentalists to develop new steady state high confinement scenarios in WEST. Overall, results show that a higher density should be aimed for high power discharges. A good starting point would be to aim a heating power of $P_{ICRH} > 3.0\ MW$ and a density $\overline{n_e} > 5.0\ 10^{19}\ m^{-3}$. The scaling law on the coupling resistance also displays how quickly this parameter diminishes with the averaged radial outer gap. Future experiments should optimize this parameter as much as possible for high-power discharges. Because closing this gap can increase the antenna limiters erosion generating W impurities, another way to improve this parameter is to shape the separatrix to better match the up-down symmetry of the antenna profile. Unfortunately, plasma shaping can be challenging. One more idea would be to reduce the cut-off density by enlarging the antenna. Modifying the ICRH antenna for a Traveling Wave Antenna (TWA) has the potential to improve the coupling efficiency and minimize edge interactions as proposed in a recent publication [22].

However, the measurement of ripple-induced fast ion losses raised new questions. In WEST, ripple-induced fast ions losses are responsible for the loss of tens of percent of the ICRH input power. In some experiments, like 55604, the ion flux can be high enough to increase the inertial baffle temperature by more than a $100°C$. A local heat flux of $q_{dep} = 3.0 \pm 0.6\ MW/m^2$ has been reached. This flux of energetic ions could cause the tungsten layer to erode. Plasma density is very small near the baffle surface. Therefore, most of the impurity ionisation takes place directly in the Scrape-Off-Layer (SOL) above the baffle and could lead to an acute contamination of the plasma core. To estimate the penetration of the eroded material, it is crucial to know what is the energy of the W atoms sputtered by high-energy H^+. Future modeling of the ripple-induced losses will help to determine this parameter. Besides, detailed investigations could be undertaken to improve the scaling law. Dedicated experiments with sufficiently high ICRH power ($P_{ICRH} > 2MW$) investigating other plasma parameters, such as the plasma current I_p and R_{1H} are to be realized for ripple-losses study. Another area of improvement is the addition of more data points to decorrelate $\overline{n_e}$ and n_H/n_D. In this way, it is possible to disentangle the influence of the isotope ratio from the plasma density, as the later parameter is expected to have a strong influence on ripple-induced fast ion losses.

6. Acknowledgements

This work has been carried out within the framework of the EUROfusion Consortium, funded by the European Union via the Euratom Research and Training Programme (Grant Agreement No 101052200

- EUROfusion). Views and opinions expressed are however those of the authors only and do not necessarily reflect those of the European Union or the European Commission. Neither the European Union nor the European Commission can be held responsible for them.

References

[1] J. Bucalossi et al. *Fusion Eng. Des.*, 89(7):907–912, 2014.

[2] C. Bourdelle et al. *Nuclear Fusion*, 55(6):063017, 2015.

[3] J. Bucalossi et al. *Nuclear Fusion*, 62(4):042007, 2022.

[4] J. Hillairet et al. *Nuclear Fusion*, 61(9):096030, 2021.

[5] V. Ostuni et al. *Nuclear Fusion*, 62(10):106034, 2022.

[6] M. Goniche et al. *Nuclear Fusion*, 62(12):126058, 2022.

[7] M. Houry et al. *Fusion Eng. Des.*, 186:113362, 2023.

[8] X. Courtois et al. *Fusion Eng. Des.*, 146:2015–2020, 2019.

[9] J. Gaspar et al. *Fusion Eng. Des.*, 149:111328, 2019.

[10] J. Gaspar et al. *Nucl. Mater. Energy*, 25:100851, 2020.

[11] N. Fedorczak et al. *Phys. Scr.*, 2020(T171):014046, 2020.

[12] L-G. Eriksson et al. *Plasma Phys. Control. Fusion*, 43(1291):1291, 2001.

[13] V. Basiuk et al. *Nuclear Fusion*, 44(1):181, 2004.

[14] V. Basiuk. HDR, Université de Marseille, 2009.

[15] V. Basiuk et al. *Fusion Technology*, 26(3P1):222–226, 1994.

[16] M. Firdaouss et al. *Fusion Engineering and Design*, 98-99:1294–1298, 2015.

[17] M.J. Mayberry et al. *Nuclear Fusion*, 30(4):579, 1990.

[18] F. Clairet et al. *Plasma Phys. Control. Fusion*, 46(10):1567, 2004.

[19] R. Bilato et al. *Plasma Phys. Control. Fusion*, 46(9):1455, 2004.

[20] C. Gil et al. *Fusion Eng. Des.*, 140:81–91.

[21] M. Greenwald. *Plasma Phys. Control. Fusion*, 44(8):R27, 2002.

[22] R. Ragona et al. *Nuclear Fusion*, 62(2):026046, 2022.

[23] M-H. Aumeunier et al. *Nucl. Mater. Energy*, 26:100879, 2021.

[24] B. Sieglin et al. *Rev. Sci. Instrum.*, 86(11):113502, 2015.

[25] J. W. David et al. Technical report, ITER, 1997.

Appendix

7. Evaluation of the baffle real surface temperature

Particles trapped in the ripple well will drift vertically until they hit the baffle and transfer their energy in the form of heat. As the tiles increase in temperature, more photons in the wavelength visible from Infra-Red (IR) cameras are emitted. An actively cooled optical endoscope looking down at the lower divertor with a resolution of 2.8 mm per pixel allows the monitoring of baffle components. The IR camera setup is detailed in reference [8]. An image of the lower Q6B sector taken with the IR upper view is given as an example in Fig. 15 for the discharge 55604 at t = +8s.

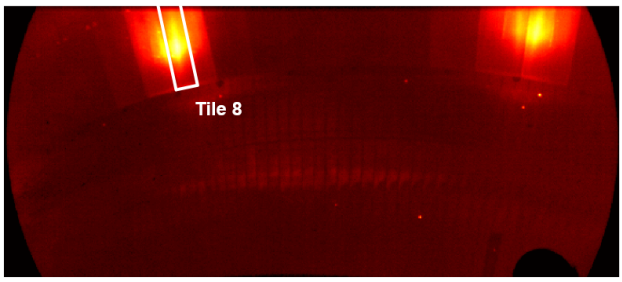

Figure 15. Image of the lower Q6B sector taken with the IR upper view. Hot areas from ripple-induced losses are visible on the baffle at the top of the image. Picture from discharge number 55604 at t = +8s.

The camera detector converts the collected photons into digital levels, and then into apparent temperature T_{BB} (BB as Black Body). The apparent temperature calculation takes into account the transmission loss of the optical line and its parasitic stray light emission in the laboratory camera calibration. However, T_{BB} translates the collected radiance into black body temperature, i.e. it is given for an emissivity $\epsilon = 1$. For a real material, the emissivity is $\epsilon < 1$, meaning the surface temperature must be higher.

The extraction of the radial profile of the apparent temperature T_{BB} is taken at the center of each tile (toroidal average over 3 pixels). The tiles' contours are defined manually on a reference image. As the camera moves between shots, a mapping independent of the heat flux pattern is done by finding the 2D correlation between the given image and the reference. The image is shifted by $(\delta x, \delta y)$ in order to maximize correlation and is assumed to be static during the pulse.

WEST's unique divertor/baffle settings (including IR and embedded thermal diagnostics) and the inertial behavior of the W coated CuCrZr tiles (temperature increase after successive plasma experiments) allows for in-situ measurement of the emissivity as in references [9, 10]. The real surface temperature T_{surf} and the apparent temperature T_{BB} can be easily linked by a linear equation via their spectral radiance:

$$L_\lambda(T_{BB}) = \epsilon * L_\lambda(T_{surf}) + L_{amb} \quad (5)$$

with $L_\lambda(T) = \frac{2hc^2}{\lambda_{IR}^5} \frac{1}{e^{\frac{hc}{\lambda_{IR} k_B T}} - 1}$ Planck's spectral radiance with h Planck's constant, c the speed of light, k_B Boltzmann constant and $\lambda_{IR} = 3.9\ \mu m$ the IR wavelength [8]. The constant L_{amb} takes into account the ambient temperature and the multiple reflections that occur in the plasma vessel. A study of these phenomena was performed on WEST and ASDEX Upgrade in reference [23].

To evaluate ϵ and L_{amb}, one must use a reference shot with known surface temperature T_{surf}. The ThermoCouples (TCs) embedded in certain tiles can be used for this purpose [9, 10]. However, to assume the TC data to be real surface temperature, the tiles must be thermalized. This assumption is true just before the plasma start-up. The tile temperature will increase during the discharge, and then cool down at the end of the experiment. However, at the start of the next plasma, the tile temperature is a little bit higher than at the start of the previous experiment. The tile starting temperature will see an overall increase during the session measured by the infrared cameras and by the embedded TC in the tiles. Thanks to this, multiple points can be measured and fitted with a linear model.

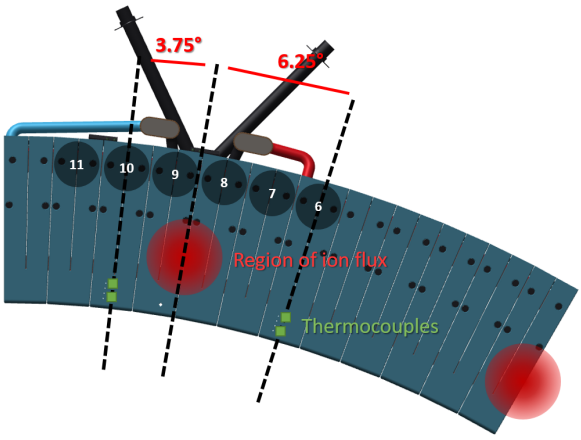

Figure 16. Design of the baffle on sector Q5A. Regions of ripple-induced losses have been represented with a red disk on tile 8 and 9 (located between two toroidal coils). TCs are shown with a green square on tile 6 and 10.

Looking at the baffle design, another obstacle emerges for our study. Fig.16 shows the design of sector

Q5A. The tiles are numbered from 1 to 12 counter-clockwise. No TC is located on tiles 8 and 9 subject to the higher ion fluxes caused by ripple-induced losses. The TCs are located on tiles 6 and 10. Because of this setup, it is not possible to directly measure the temperature on the tiles of interest. However, it is possible to assume that the baffle temperature is uniform in certain conditions. For high-power sessions not using ICRH, the baffle temperature will increase uniformly (mainly due to radiation). The other assumption will be that the emissivity profile of the tile does not change over the campaign. This assumption will be verified later. TC on tile 10 has been chosen for its proximity with the losses region.

As an example, Fig.17 shows the evolution of the luminance for tile 8 at R= 2.53 m from discharges 55764 to 55890. This corresponds to a "high energy" session using very high Lower-Hybrid (LH) power for a long duration without ICRH power (sometimes exceeding 50s).

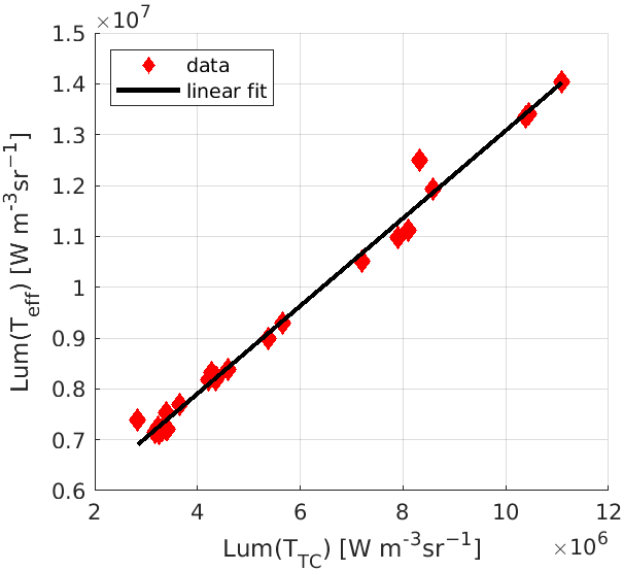

Figure 17. Linear regression of the effective luminance compared with the TC luminance. This regression allows to get the emissivity ϵ and constant L_{amb} for one point of the tile. Taken from discharges 55764 to 55890 for tile 8 at R=2.53m.

The emissivity and the background reflection can be calculated from the linear regression of the luminance of T_{BB} and T_{TC} for each pixel of the tiles. To verify that the emissivity profile is constant in time, the same process is applied to other sessions. In Fig.18, the emissivity and the ambient background reflection profile have been calculated for several shots. The tiles' emissivity profile has been evaluated and considered constant during the whole campaign taking the average profile. The spread (± 0.1 for ϵ and $\pm 10^6$ $Wm^{-3}sr^{-1}$ for L_{amb}) is taken into account in the uncertainty calculation.

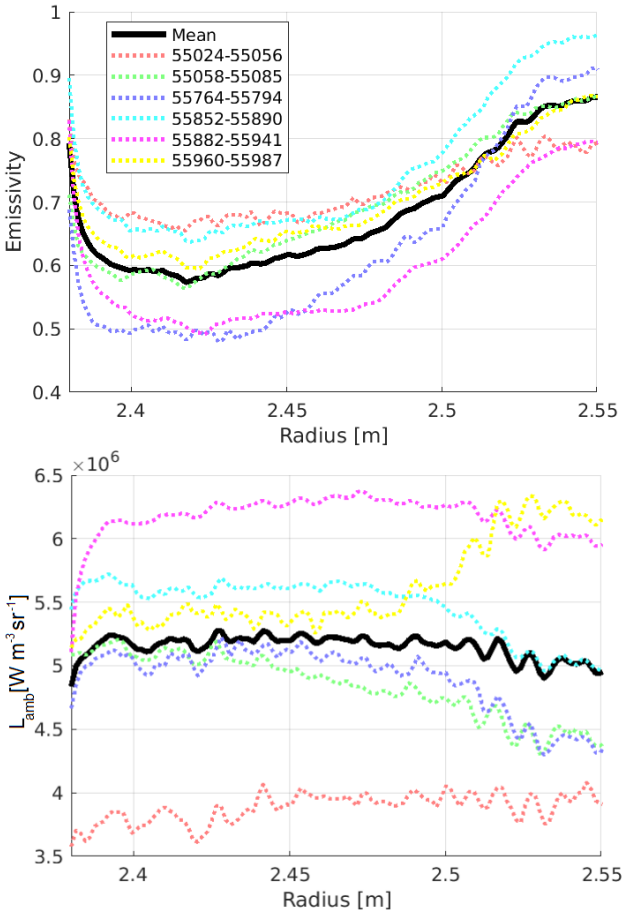

Figure 18. Top: Emissivity (ϵ) profile. Bottom: Ambient background reflection (L_{amb}) profile. For tile 8.

During campaign C4, in the region of ripple-induced losses, the emissivity has been calculated to be in average $\epsilon = 0.62 \pm 0.10$, and the ambient background reflection is equal to $C = (5.2 \pm 1.0) 10^6$ W m^{-3} sr^{-1}. The temperature radial profile at the center of the tile 8 will be used to evaluate the heat flux deposited on the baffle.

8. From infra-red thermography to fast ion heat flux

From the evolution of the temperature profile, the fast ion flux can be evaluated using the code TEDDY. TEDDY is a thermography inversion algorithm developed for the physical exploitation of WEST IR data of uncooled graphite tiles coated with $12\mu m$ of tungsten located on the lower divertor [11]. For this work, the code has been adapted for the IR thermography of the baffle. In TEDDY, as in THEODOR [24], the heat is considered to mostly diffuse through the tile along two main directions: the radial direction along the profile of deposited heat

flux and the depth of the tile, perpendicular to the previous direction. Along these two directions, the heat equation reads:

$$\rho C_p(T)\partial_t T_{surf} = \nabla \cdot (\lambda \nabla T_{surf} + q_{dep})$$

where $\rho = 8835 \pm 25\ kg/m^3$ is the volumetric mass of the material composing the tile, $C_p = 400 \pm 10\ J/(kg\ K)$ the specific heat capacity and $\lambda = 335 \pm 30\ W/(m\ K)$ the thermal conductivity of the material. The thermal properties of the material that compose the tile comes from ITER material handbook [25]. T_{surf} denotes the local surface temperature of the tile in $°C$ and q_{dep} the deposited heat flux in W/m^2. The numerical scheme can solve either in the forward ($q_{dep} \rightarrow T_{surf}$) or in the reverse model ($T_{surf} \rightarrow q_{dep}$), which is the one of interest for this study.

Some uncertainties have been introduced by the input parameters. The IR cameras during the C4 campaign have a 10% uncertainty on the apparent temperature T_{BB} measurement, but this has a negligible impact on q_{dep} because Planck's luminance mitigates these differences. The emissivity and the ambient background reflection can vary throughout the campaign as mentioned previously (respectively by $\epsilon \pm 0.1$ and $C_{amb} \pm 10^6\ J/(kg\ K)$). Finally, the material properties measurement of CuCrZr has been considered constant but can change with the temperature. Because the analytical calculation of the uncertainty is not possible, a Monte Carlo scheme has been used to evaluate the variation in the calculation of q_{dep}.

9. Error related to the Gaussian fit of the heat flux profile

In section 2.2, the power deposition profile q_{dep} is fitted with a 2D Gaussian allowing the reduction of the number of parameters, the signal noise and taking into account the ion flux deposited outside the camera's field of view by extending the profile. For making this argument, an evaluation of the error must be performed in order to assess the worth of this simplification. For concision, only pulse 55604 will be treated here. All the numbers and graphs are from this discharge.

First, the radially integrated power flux is compared with and without the Gaussian fit in order to assess the validity of this approximation. Along the profile, the difference in the radially integrated power flux is minor between the measurement and the Gaussian fit. During the ICRH power window, the median relative error between the two signals is 1.5%, despite a few outliers when the ICRH power drops. This observation confirms that the deviation is sufficiently small to evaluate the power deposition as a Gaussian function. Extending the profile with the fit gives a median increase of 9.0% on the radially integrated power flux. We conclude that the error in the estimate of the deposited power done when neglecting the region outside the camera view is bigger than the error due to the deviation of the Gaussian from the measured profile. An example of profile is shown in Fig.19 for t=5.78s.

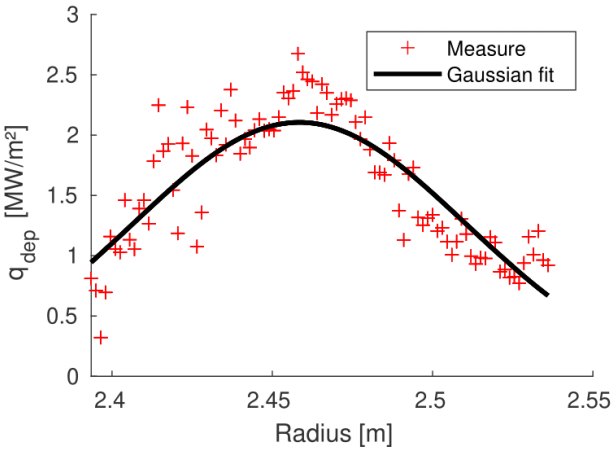

Figure 19. Power flux profile during pulse 55604 at t=5.78s.

Then, to integrate q_{dep} on a 2D profile and obtain P_{ripple}, the power deposition is supposed to be symmetric by rotation around the peak power flux. Because the fitting works better with higher flux and because the integral of the 2D Gaussian follows σ^2, we consider the width of the power deposition σ to be constant during the pulse to limit the fluctuations. To compute its value, a median is taken from the Gaussian fits where the Root Mean Square Error (RMSE) is below a threshold and the ICRH power is above 1 MW. Fig.20 shows the evolution of the width of the Gaussian fit through time.

It appear that σ stabilises when the measured ripple-induced losses are important. This is due to a better fitting resulting in a lower RMSE. The red markers shows the width values from which the median is taken for the estimation of the pulse's σ, supposed to be constant. The values are taken at the 50 timestamps where the RMSE is the lowest. For pulse 55604, the median value is $\sigma = 5.51 \pm 0.64\ cm$. The temporal standard deviation is 11.6% of the computed median σ. This value is computed for all discharges and added to the estimation of the error bars shown in Fig.6

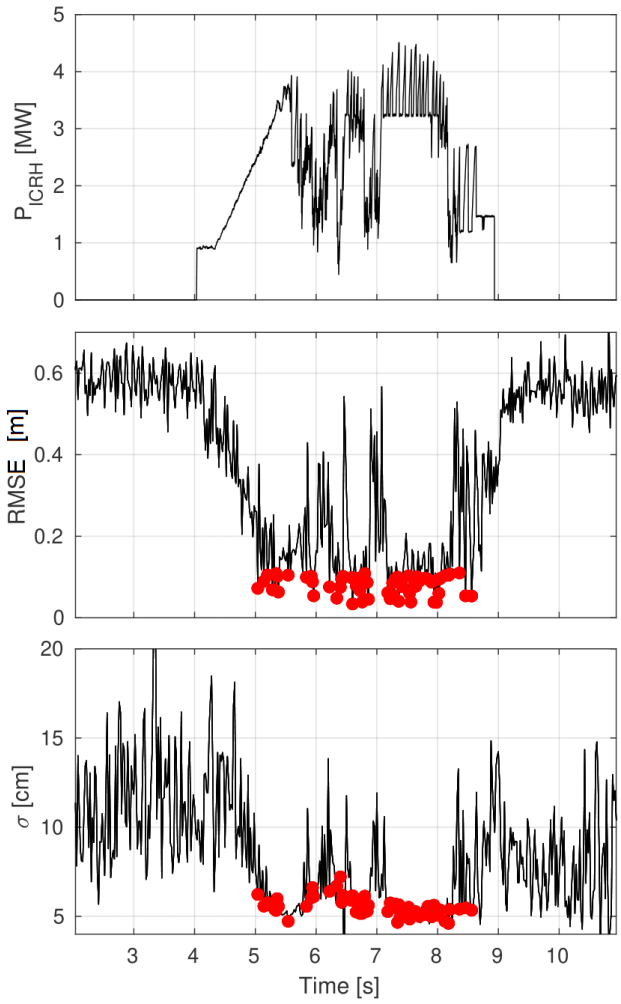

Figure 20. Top: ICRH power signal of pulse 55604. Middle: Evolution of the RMSE of the Gaussian fit, with the red markers corresponding to the 50 points with lowest values. Bottom: Evolution of the width of the Gaussian fit σ, with red markers highlighting the 50 values taken for the estimation of the pulse's σ, supposed to be constant.